



Full length article

Phase-field investigation on the peritectic transition in Fe-C system

Yuhan Cai^{a,*}, Fei Wang^{a,1}, Zihan Zhang^a, Britta Nestler^{a,b,2}^a Institute of Applied Materials, Karlsruhe Institute of Technology (KIT), Strasse am Forum 7, Karlsruhe 76131, Germany^b Institute of Digital Materials Science, Karlsruhe University of Applied Sciences, Moltkestrasse 30, Karlsruhe 76133, Germany

ARTICLE INFO

Article history:

Received 21 January 2021

Revised 15 July 2021

Accepted 30 July 2021

Available online 11 August 2021

Keywords:

Fe-C binary system

Phase-field model

Dynamic contact angle

Peritectic transition

ABSTRACT

We adopt a thermodynamically consistent multi-phase, multi-component phase-field model to investigate the morphological evolution of peritectic transition in carbon steel through 2-D and 3-D simulations. By using phase-field method, we rationalize the peritectic solidification in both 2-D and 3-D simulations under different liquid supersaturations as well as on the δ particle with distinct microstructures. Through the comparison between 2-D and 3-D simulation results, we clarify the reason for the different growth rate of γ phase in two and three dimensions. In 3-D simulation, we observe the unequal growth rate of γ phase in radial and axis directions. In addition, a novel measurement method is proposed to determine the dynamic contact angle. We anticipate that the simulation results can be applied to interpret the isothermal peritectic transition with a liquid supersaturation in alloys.

© 2021 The Authors. Published by Elsevier Ltd on behalf of Acta Materialia Inc.
This is an open access article under the CC BY-NC-ND license
(<http://creativecommons.org/licenses/by-nc-nd/4.0/>)

1. Introduction

High-strength steels within the peritectic composition range are used in a broad variety of engineering applications due to its outstanding mechanical properties [1–3]. However, the defects generated by the peritectic transition during solidification, such as surface depressions, cracks, and breakouts, have a crucial damage on mechanical properties and thereby limit the utilization of steels [4–7]. In order to avoid these defects in steels, numerous investigations on the microstructural evolution in peritectic transition have been conducted in the past decades.

The peritectic phase transition in carbon steel involves the peritectic reaction ($L + \delta \rightarrow \gamma$) and subsequent peritectic transformations ($L \rightarrow \gamma$ and $\delta \rightarrow \gamma$). Many different mechanisms have been proposed via experimental observations to explain the details of this phase transition. Shibata et al. [8] investigated the peritectic transition in carbon steel by using a confocal scanning laser microscope (CSLM) and proposed that the growth of the γ phase is not controlled by carbon-diffusion but by either a massive transformation or a direct solidification from the liquid. In the study of peritectic transition, Griesser et al. observed three different modes,

including a diffusion controlled mode, a cellular/dendritic peritectic transformation mode, and a massive transformation mode, by the use of a concentric solidification technique [9]. Nassar et al. [10] experimentally observed that surface tension plays a vital role in the governing mechanism of γ phase. Owing to the complexity of the peritectic transition, the explanation about the growth mechanisms is not entirely consistent.

Considering the daunting task of statistical and theoretical investigations by precisely controlled experiments, it is of great significance and feasibility to gain insight into the peritectic transition by using computational materials simulations. The phase-field model has been proven to be a powerful modeling technique to simulate the microstructural evolution in many alloy systems [11–13], including peritectic alloys. By using phase-field method, Tiaden et al. [14] studied the engulfing microstructure, in which the peritectic phase grows over the pro-peritectic phase. Dobler et al. [15] documented another possible growth morphology in peritectics, namely coupled growth of lamellae or rods like in eutectics, and clarified the main differences between this analogues morphology in peritectics and eutectics. In addition, the peritectic transition in carbon steels is explored by phase-field modeling to clarify its underlying growth mechanism [16–18]. Ohno and Matsuura [19] investigated the γ growth at different undercoolings by using phase-field model and confirmed previous experimental observations proposed by Hillert [20] that the re-melting of δ phase in the vicinity of triple junction affects the peritectic reaction rate. This phenomenon has been also confirmed by other phase-field

* Corresponding author.

E-mail addresses: yuhan.cai@kit.edu (Y. Cai), fei.wang@kit.edu (F. Wang), britta.nestler@kit.edu (B. Nestler).¹ +49 721 608 41453.² +49 721 608 45310.

modeling studies [21,22]. Owing to their focus on the mechanisms of peritectic reaction, these studies investigated the growth of γ phase on a planar δ phase at different undercoolings in 2-D simulations. However, there is a paucity of researches discussing the curvature effect of δ particle on the growth of γ phase as well as on the growth process after the complete engulfment of δ particle. Moreover, in comparison with 2-D simulations, the curvature effect in an extra direction in 3-D should also be taken into consideration. As a supplement to the work of Ohno et al, we presently explore the morphological evolution of γ phase on a spherical δ particle in 2-D and 3-D simulations. In the most of above mentioned studies, more attention were paid to the peritectic transition at different undercoolings, while research on the peritectic transition caused by the supersaturation still has a gap.

The early phase-field models, proposed by Karma [23] and Wheeler et al. [24], were used to simulate alloy solidification. These models applied a dual phase-field model to describe the solid and liquid phases and are coupled with Cahn-Hilliard model for demixing in solid phase. However, they are restricted to emulate the three-phase transition. In order to solve this problem, a multi-phase model was developed [14,25]. In this multi-phase model, each phase is identified with an individual phase field parameter φ_α . Nestler and Wheeler [26] formulated a phase-field approach based on interpolating the free energy density to simulate the solidification process for binary eutectic and peritectic alloy systems, by setting up suitable values for the latent heats and temperature. This model in combination with a cubic anisotropy function was applied by Choudhury et al. [27] to emulate the solidification in Fe-C. Due to a common idea that the driving force for a phase transformation is the difference in the grand potentials between phases, Choudhury and Nestler reformulated a multi-phase-field model based on the grand-potential functional [28]. Moreover, the anomalous interface effects were observed in several numerical investigations by using the phase-field model, when the interface width was extended artificially and the solute has unequal diffusivities between phases [29–31]. In order to eliminate these abnormal effects, an anti-trapping current was proposed into the diffusion equation by Karma [32]. In the past decades, the static contact angle is determined by the thermodynamic equilibrium at the triple junction between three distinct phases, described by Young's law. However, the dynamic contact angle deviates from the Young's law under the influence of the interface motion, which is observed in several experimental and numerical observations about spreading of fluids [33–35]. Similarly, the occurrence of the phase transition is accompanied with the movement of interfaces. Hence, the dynamic contact angle may also deviate from Young's law during the phase transition. In the previous study of Ohno and Matsuura, the measurement methods of the dynamic contact angle cannot determine the contact angle precisely and the value of the contact angle is significantly affected by the different selecting criteria [19]. In order to better explore the dynamic contact angle in peritectic transition, a novel measurement method for a dynamic contact angle should be proposed.

As mentioned above, the peritectic transition is frequently found in different alloys, e.g. Cu-Sn [36], Ag-Sn and Cd-Ag [37], and Fe-Co [38], and the phase-field method is applied to research this phase transition since quite early on. However, the understanding of peritectic transition in alloy solidification, especially from numerical studies, is considerably limited compared to other common phase transitions in alloy, such as eutectic transition. The relatively small amount of numerical investigations on the peritectic transition is likely to be caused by the following reasons: (i) In comparison with eutectic transition, there are much greater variety of growth modes in peritectic transformation, e.g., diffusion control mechanism, δ -ferrite remelting mechanism, and massive transformation mechanism [9,39]. (ii) According to the previous experi-

mental and numerical observations [8,27], the growth rate of γ -phase after the complete engulfment of the δ particle decreases significantly, and consequently the simulation of whole process requires a high amount of computational effort, especially for a 3-D simulation. (iii) Most previous studies focus on directional solidification in peritectic transformation where the steady-state growth is rarely achieved [40]. (iv) The paucity of 3D phase-field modeling of peritectic transition in mesoscopic scale is probably due to the capability of the phase-field model before the invention of the thin interface analysis as well as the decoupling of the interfacial energy from the interface width in the grand potential formalism.

In the present work, we shed light on the microstructural evolution of peritectic transition in carbon steel by using phase-field method and propose a new measurement method to determine the dynamic contact angle. A common agreement is reached through several studies that the peritectic transition in Fe-C alloys at low driving force (e.g. at low undercoolings) is controlled by carbon diffusion [9,10,41]. Therefore, in the modeling section, we present a phase-field model formulation in 3-D, added with an anti-trapping current and coupled with a diffusion-equation, to simulate the occurrence of phase transition and the growth of intermetallic compound. By using this phase-field method, we simulate the evolution of γ phase in both 2-D and 3-D simulations under different liquid supersaturations as well as on the δ particle with distinct microstructures. All large domain simulations in 2-D and 3-D are performed in parallel computing on high performance computers. By analyzing the concentration distribution and morphological evolution, we clarify the underlying mechanisms of the peritectic transition in carbon steel.

2. Binary phase diagram of Fe-C system

Fig. 1(a) shows the reconstructed Fe-C binary phase diagram based on the thermodynamic database published in Ref. [42]. According to this phase diagram, γ -Fe is produced by a peritectic reaction between liquid and δ -Fe phases at the peritectic temperature $T_p = 1767$ K, $L + \delta - \text{Fe} \rightarrow \gamma - \text{Fe}$. In the present study, we simulate this peritectic reaction at the temperature $T = 1757$ K, which is 10 K below T_p , as displayed by the red dashed line in Fig. 1(a). Here, $c_e^{\gamma,L}$ and $c_e^{L,\gamma}$ represent the equilibrium concentration in γ phase with respect to liquid phase and the equilibrium concentration in liquid phase with respect to γ phase at $T = 1757$ K, respectively. In order to simulate this peritectic transition, we fit the Gibbs free energies of liquid-, γ -, and δ -phases based on the CALPHAD database [42], by using the least square method. The fitted Gibbs free energy curves are displayed in Fig. 1(b). The thermodynamic equilibrium between two phases is given by the common tangent construction between two Gibbs energy curves, as illustrated by the pink or olive dashed line in Fig. 1(b). The equilibrium chemical potentials correspond to the slopes of the common tangent lines. This fitting method results in exact equilibrium concentrations between each pairwise phases (L/γ - and δ/γ -phase), which are in accordance with experimental data.

3. Phase-field model

In the present study, we use a phase-field model with the grand-potential formulation, which is proposed by Choudhury and Nestler [28], to investigate the microstructural evolution in peritectic transition. For a N-phase and K-component system, the bulk free energy density of the phase α is formulated as

$$f^\alpha = f^\alpha(c_1^\alpha, \dots, c_k^\alpha, \dots, 1 - \sum_{i=1}^{K-1} c_i^\alpha), \alpha \in [1, N], k \in [1, K]. \quad (1)$$

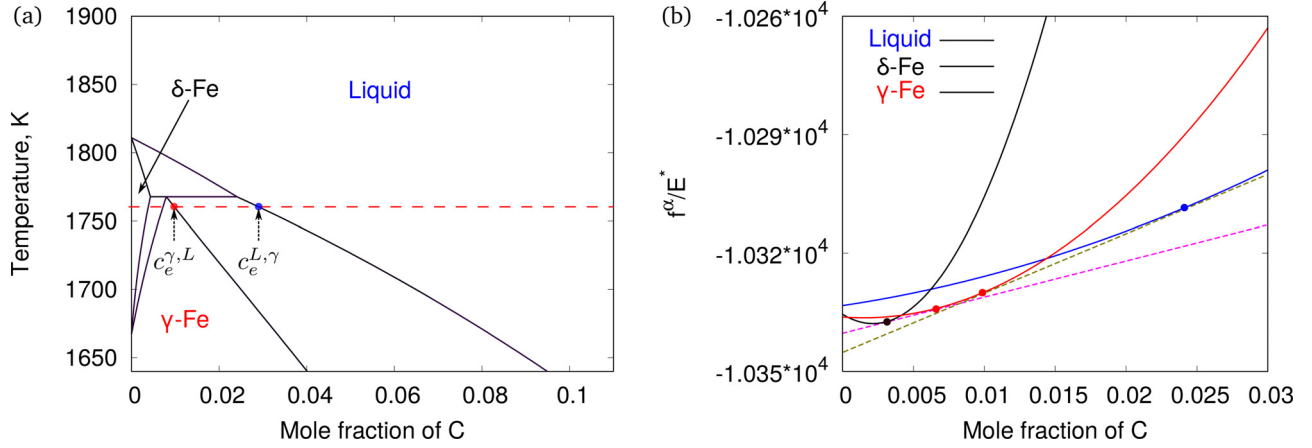


Fig. 1. (a) Phase diagram of the Fe-C system. We consider the reaction at the temperature $T = 1757$ K, as indicated by the red dashed line. (b) The fitted dimensionless free energy f^α/E^* as a function of concentration, at a fixed temperature $T = 1757$ K, where $E^* = 1 \times 10^6$ J/m³. $\alpha =$ liquid, δ -Fe, and γ -Fe, respectively. (For interpretation of the references to colour in this figure legend, the reader is referred to the web version of this article.)

The chemical potential for the α phase is calculated by the following equation:

$$\mu_k^\alpha = \frac{\partial f^\alpha}{\partial c_k^\alpha}. \quad (2)$$

The grand chemical potential is defined as

$$\Psi^\alpha(\boldsymbol{\mu}) = f^\alpha(\mathbf{c}^\alpha(\boldsymbol{\mu})) - \langle \boldsymbol{\mu}^\alpha, \mathbf{c}^\alpha \rangle, \quad (3)$$

where the concentration vector is defined as $\mathbf{c}^\alpha = (c_1^\alpha, \dots, c_{K-1}^\alpha)$ and the chemical potential vector is written as $\boldsymbol{\mu}^\alpha = (\mu_1^\alpha, \dots, \mu_{K-1}^\alpha)$. When the phases are in thermodynamic equilibrium, the chemical potential of each phase has the same value, thereby the chemical potential vector can be described as $\boldsymbol{\mu}^\alpha = \boldsymbol{\mu} = (\mu_1, \dots, \mu_{K-1})$. The mathematical symbol $\langle \cdot, \cdot \rangle$ represents a scalar product.

In this model, an order parameter φ_α is introduced to represent the local volume fraction of the α phase, whose value characterizes the phase state of the system in time and space. In addition, we use a diffuse interface to separate two distinct phases α and β . Hence, we set the order parameter $\varphi_\alpha = 1$, $0 < \varphi_\alpha < 1$, $\varphi_\alpha = 0$ in the bulk phase α , in the diffuse interface, and in other phases, respectively. The phase-field vector $\boldsymbol{\varphi} = (\varphi_1, \dots, \varphi_N)$ is used to characterize the phase state of the system. The grand chemical potential in the diffuse interface is interpolated in terms of the individual phases as

$$\Psi(\boldsymbol{\varphi}, \boldsymbol{\mu}) = \sum_{\alpha=1}^N \Psi^\alpha(\boldsymbol{\mu}) h(\varphi_\alpha), \quad (4)$$

where $h(\varphi_\alpha)$ is a cubic interpolation function defined as $h(\varphi_\alpha) = \varphi_\alpha^2(3 - 2\varphi_\alpha)$ and satisfies $h(0) = 0$ and $h(1) = 1$. With the aid of Eq. (3), we differentiate both sides of Eq. (4) with respect to μ_i yielding

$$\mathbf{c}(\boldsymbol{\varphi}, \boldsymbol{\mu}) = \sum_{\alpha=1}^N \mathbf{c}^\alpha(\boldsymbol{\mu}) h(\varphi_\alpha), \quad (5)$$

where the concentration vector is defined as $\mathbf{c} = (c_1, \dots, c_{K-1})$.

In accordance with the basic thermodynamic law, the fundamental idea of using the phase-field method to illustrate the phase transition process in a multiphase system is such as to minimize the grand potential functional $d\Omega/dt \leq 0$, which is achieved with the following formulation:

$$\Omega(\boldsymbol{\varphi}, \boldsymbol{\mu}) = \int_V \left[\epsilon a(\boldsymbol{\varphi}, \nabla \boldsymbol{\varphi}) + \frac{1}{\epsilon} w(\boldsymbol{\varphi}) + \Psi(\boldsymbol{\varphi}, \boldsymbol{\mu}) \right] dx. \quad (6)$$

Here, V is the volume occupied by the system, and ϵ is a length parameter, which determines the width of the diffuse interface.

The first term in Eq. (6) represents the gradient energy density that is formulated as

$$a(\boldsymbol{\varphi}, \nabla \boldsymbol{\varphi}) = \sum_{\alpha < \beta} \gamma_{\alpha\beta} [a_{\alpha\beta}(\mathbf{q}_{\alpha\beta})]^2 |\mathbf{q}_{\alpha\beta}|^2, \quad (7)$$

where $\gamma_{\alpha\beta}$ is a coefficient defining the surface energy of the $\alpha - \beta$ interface, and $\mathbf{q}_{\alpha\beta}$ is the generalized asymmetric gradient vector, which is written as: $\mathbf{q}_{\alpha\beta} = \varphi_\alpha \nabla \varphi_\beta - \varphi_\beta \nabla \varphi_\alpha$. Here, the anisotropy of solid phases is not taken into consideration, hence $a_{\alpha\beta}(\mathbf{q}_{\alpha\beta})$ is set as 1.

The second term in Eq. (6) is an obstacle potential, which is expressed as

$$w(\boldsymbol{\varphi}) = \frac{16}{\pi^2} \sum_{\alpha < \beta} \gamma_{\alpha\beta} \varphi_\alpha \varphi_\beta + \sum_{\alpha < \beta < \delta} \gamma_{\alpha\beta\delta} \varphi_\alpha \varphi_\beta \varphi_\delta. \quad (8)$$

Here, the higher order term $\gamma_{\alpha\beta\delta}$ suppresses spurious contributions of third phases in the binary interfaces. The temporal phase-field evolution equation is derived by the variational approach and writes as

$$\tau_{\alpha\beta} \epsilon \frac{\partial \varphi_\alpha}{\partial t} = \epsilon \left[\frac{\partial a(\boldsymbol{\varphi}, \nabla \boldsymbol{\varphi})}{\partial \varphi_\alpha} - \nabla \cdot \frac{\partial a(\boldsymbol{\varphi}, \nabla \boldsymbol{\varphi})}{\partial \nabla \varphi_\alpha} \right] - \frac{1}{\epsilon} \frac{\partial w(\boldsymbol{\varphi})}{\partial \varphi_\alpha} - [\Psi^\alpha(\boldsymbol{\mu}) - \Psi^\beta(\boldsymbol{\mu})] h'(\varphi_\alpha) - \lambda, \quad (9)$$

$\alpha = 1, \dots, N, \beta \neq \alpha,$

whereby λ is a Lagrange multiplier ensuring $\sum_{\alpha=1}^N \varphi_\alpha = 1$. The parameter $\tau_{\alpha\beta}$ is a relaxation constant at the α/β interface, which is discussed later in this section.

Furthermore, the total amount of solute in the system is conserved. Therefore, we introduce a diffusion equation, which follows Fick's law. As the flux in the diffuse interface of phase-fields differ from the sharp interface limit, an anti-trapping current is added in this solute conservation equation. The evolution equation for the concentration fields is derived as [28,43]

$$\frac{\partial \mathbf{c}}{\partial t} = \nabla \cdot \left[\mathbf{M}(\boldsymbol{\varphi}, \boldsymbol{\mu}) \nabla \boldsymbol{\mu} - \mathbf{J}_{at} \right], \quad (10)$$

where $\mathbf{M}(\boldsymbol{\varphi}, \boldsymbol{\mu}) = \sum_{\alpha=1}^N \mathbf{M}^\alpha(\boldsymbol{\varphi}, \boldsymbol{\mu}) h(\varphi_\alpha)$ is the mobility. The mobility of atoms in α phase \mathbf{M}^α is defined as

$$\mathbf{M}^\alpha = \frac{\mathbf{D}^\alpha}{\frac{\partial \boldsymbol{\mu}}{\partial \mathbf{c}^\alpha}}, \quad (11)$$

where \mathbf{D}^α is the diffusivity matrix in α phase. In this paper, we only state the result of the anti-trapping current in the phase-field

simulation and refer to another paper for details of the asymptotic and derivation [28]. The anti-trapping current is defined as

$$J_{at} = \frac{\pi\epsilon}{4} \sum_{\alpha=1}^N \frac{h(\varphi_\alpha)(1-h(\varphi_\alpha))}{\sqrt{\varphi_\alpha^0(1-\varphi_\alpha^0)}} \frac{\partial\varphi_\alpha}{\partial t} \left(\frac{\nabla\varphi_\alpha}{|\nabla\varphi_\alpha|} \cdot \frac{\nabla\varphi_L}{|\nabla\varphi_L|} \right) \times \left(\mathbf{c}^L(\boldsymbol{\mu}, T) - \mathbf{c}^\alpha(\boldsymbol{\mu}, T) \right) \otimes \frac{\nabla\varphi_\alpha}{|\nabla\varphi_\alpha|}, \quad (12)$$

where φ_α^0 is the lowest order solution of the phase-field equation, \mathbf{c}^L and \mathbf{c}^α is the concentration in liquid and solid phase, respectively. It should be noted that the diffusion coefficient in the liquid phase \mathbf{D}^L is much larger than the one in the solid phases \mathbf{D}^α , thereby the anti-trapping current with an assumption of one sided diffusion is adopted in the present study.

According to Eq. (5), the time derivative of the concentration is written as

$$\begin{aligned} \frac{\partial\mathbf{c}}{\partial t} &= \sum_{\alpha=1}^N \mathbf{c}^\alpha(\boldsymbol{\mu}) \frac{\partial h(\varphi_\alpha)}{\partial t} + \sum_{\alpha=1}^N \frac{\partial\mathbf{c}^\alpha(\boldsymbol{\mu})}{\partial t} h(\varphi_\alpha) \\ &= \sum_{\alpha=1}^N \mathbf{c}^\alpha(\boldsymbol{\mu}) h'(\varphi_\alpha) \frac{\partial\varphi_\alpha}{\partial t} + \sum_{\alpha=1}^N \frac{\partial\mathbf{c}^\alpha}{\partial\boldsymbol{\mu}} h(\varphi_\alpha) \frac{\partial\boldsymbol{\mu}}{\partial t}. \end{aligned} \quad (13)$$

Through a combination of Eqs. (10) and (13), the evolution equation for the chemical potential is formulated as

$$\begin{aligned} \frac{\partial\boldsymbol{\mu}}{\partial t} &= \left[\sum_{\alpha=1}^N \frac{\partial\mathbf{c}^\alpha(\boldsymbol{\mu})}{\partial\boldsymbol{\mu}} h(\varphi_\alpha) \right]^{-1} \\ &\cdot \left[(\nabla \cdot (\mathbf{M}(\boldsymbol{\varphi}, \boldsymbol{\mu}) \nabla\boldsymbol{\mu} - J_{at})) - \sum_{\alpha=1}^N \mathbf{c}^\alpha(\boldsymbol{\mu}) h'(\varphi_\alpha) \frac{\partial\varphi_\alpha}{\partial t} \right]. \end{aligned} \quad (14)$$

Hereafter, we restrict our discussion for the case of a binary alloy where the concentration c is the concentration of carbon and μ is the corresponding chemical potential. Hence, there is only one independent inter-diffusivity in the system and the mobility \mathbf{M}^α is written as $M^\alpha = D^\alpha \frac{\partial\mathbf{c}}{\partial\boldsymbol{\mu}}$.

Next, we relate the modeling parameter $\tau_{\alpha\beta}$ for the time relaxation to the physical parameter of kinetic coefficient ξ . In literature, there are two approaches to estimate the value of $\tau_{\alpha\beta}$ in terms of ξ . The first one is in the context of the sharp-interface limit, where the chemical potential within the diffuse interface is almost constant. To achieve this, the interface width in the phase-field model should be much less than the capillary length. Hence, the interface width in the phase-field method is typically in nanometer scale. In this way, it is impractical for the numerical simulation to simulate microstructure evolution in mesoscopic scale, especially in 3D, since the grid resolution and the time scale of the phase-field model are both related with the interface width. For instance, it would require ten thousand cubic grid cells in 3D to simulate a domain with a size of $10 \times 10 \times 10 \mu\text{m}^3$, which is extremely challenging for the present computational capability even with high performance computing technique. To overcome this difficulty, a second way to relate $\tau_{\alpha\beta}$ in terms of ξ is the so-called thin-interface analysis, as derived in Refs. [32,44–47]. Benefiting from the decoupling of the interface width from the interfacial energy for relatively small driving force (equilibrium solidification), the interface width in the second approach can be set arbitrarily large, e.g. 100 nm. For such a large interface width, it is still possible to obtain a physical value for the interfacial energy and replicate the classic Stefan problem. This large interface width is beyond the physical meaning of realistic value but is indeed a significant modeling approach to perform large scale 3D simulations. However, an arbitrary enlargement of the interfacial width results

in some artifacts for those properties, such as interfacial diffusion, which are proportional to the interfacial width. To eliminate these artifacts, an additional constraint, namely, the aforementioned anti-trapping current is applied.

In the following, we exemplarily illustrate the derivation of the modeling parameter $\tau_{\gamma L}$ at γ/L interface. By asymptotic expansions of phase-field variable and chemical potential with considering the anti-trapping current, the deviation of the chemical potential from the equilibrium value in the thin interface analysis is expressed as

$$\Delta\mu := \mu - \mu_e = \mu^0 - \mu_e + \epsilon\mu^1, \quad (15)$$

where μ^0 and μ^1 are the solutions of the chemical potential in the sharp and thin interface analysis, which are obtained by analyzing the phase-field equation in the order of ϵ^0 and ϵ^1 , respectively. μ_e is the equilibrium chemical potential. The departure from the equilibrium chemical potential in the sharp-interface limit $\mu^0 - \mu_e$ is written as

$$\mu^0 - \mu_e = \frac{-\tau_{\gamma L} V}{c^L(\mu_e, T) - c^\gamma(\mu_e, T)}, \quad (16)$$

where V is the interface velocity. The chemical potential μ^1 is formulated as

$$\mu^1 = \frac{c^L(\mu^0, T) - c^\gamma(\mu^0, T)}{D^L \frac{\partial c^L(\mu^0, T)}{\partial\mu}} V (M + F). \quad (17)$$

Here, M and F are solvability integrals equating to 0.063828 and 0.158741, respectively. Substituting Eq. (16) and Eq. (17) into Eqs. (15) and comparing Eqs. (15) with the Gibbs-Thomson equation $\Delta T = \xi V$ for an one-dimensional setup, where $\Delta T = m_L \frac{\partial c^L(\mu_e, T)}{\partial\mu} \Delta\mu$ (m_L is the slope of the liquidus), the modelling parameter $\tau_{\gamma L}$ is related to the kinetic coefficient ξ . In this work, we set the kinetic coefficient ξ to be zero to estimate the modelling parameter $\tau_{\gamma L}$, namely,

$$\tau_{\gamma L} = \epsilon \frac{[c^L(\mu_e, T) - c^\gamma(\mu_e, T)][c^L(\mu^0, T) - c^\gamma(\mu^0, T)]}{D^L \frac{\partial c^L(\mu^0, T)}{\partial\mu}} (M + F). \quad (18)$$

The reason for setting $\xi = 0$ is two-fold. Firstly, in 2D and 3D, apart from the kinetic undercooling, the Gibbs-Thomson equation has an additional contribution from the curvature, namely, $\Delta T = \xi V + \Gamma\kappa$, where Γ is the Gibbs-Thomson coefficient and κ is the curvature. The kinetic coefficient ξ for alloys is typically in the scale of $1 \times 10^{-5} \text{Ks}/(\mu\text{m})$ [48,49]. For equilibrium solidification, this kinetic undercooling is much less than the curvature undercooling. Secondly, in comparison with the parameter $\tau_{\alpha\beta}$ corresponding to a non-zero kinetic coefficient, a modelling parameter $\tau_{\alpha\beta}$ for a zero kinetic coefficient leads to a less transient time and a faster convergence of the simulation to the steady state, which is an additional advantage to simulate large 3D simulations.

We initially fill a semicircular γ nucleus at the interface between the liquid and δ phases. The interface thickness is set to be $1.5 \mu\text{m}$ in order to keep the simulation stable. The concentration of C in γ is set to be 0.006785, which is the equilibrium concentration with δ phase at the temperature of 1757 K. The carbon concentration in the δ phase is 0.003159 implying a supersaturation of $\Delta_{\gamma/\delta} = 0.027$. Due to the constant concentration in δ phase, all supersaturation hereafter refers specifically to the supersaturation in liquid. The other simulation parameters are tabulated in Table 1. In the following discussion, we simulate the growth of γ -phase with different supersaturation in liquid and its development on the δ -particle in various size. Neumann boundary conditions are applied in the present simulations. The supersaturation in liquid is defined

Table 1
Parameters for the phase-field simulations.

Symbol	Description	Value
Δt	Time step	$1 \times 10^{-6} \text{s}$
Δx	Space step	$1 \times 10^{-7} \text{m}$
$\sigma_{\gamma\delta}$	Interfacial energy of the γ/δ interface	0.370Jm^{-2}
$\sigma_{\gamma L}$	Interfacial energy of the γ/L interface	0.319Jm^{-2}
$\sigma_{\delta L}$	Interfacial energy of the δ/L interface	0.204Jm^{-2}
D_L	Diffusion coefficient in the L-phase	$5.2 \times 10^{-7} \exp(-5.0 \times 10^4 / (RT)) \text{m}^2 \text{s}^{-1}$ [19]
D_γ	Diffusion coefficient in the γ -phase	$D_L \times 0.01$
D_δ	Diffusion coefficient in the δ -phase	$D_L \times 0.01$
R	Gas constant	8.314J/molK

as

$$\Delta = \frac{c_0^L - c_e^{L,\gamma}}{c_e^{\gamma,L} - c_e^{L,\gamma}}, \quad (19)$$

where $c_e^{L,\gamma}$ is the solute concentration in the liquid phase in equilibrium with the γ -phase and $c_e^{\gamma,L}$ is the carbon concentration in the γ phase in equilibrium with the liquid (see Fig. 1(a)). c_0^L represents the initial carbon concentration in liquid phase. In the following discussion, the supersaturation Δ of 0.352, 0.281, 0.211, 0.141, and 0.071 corresponds to the initial carbon concentration in liquid c_0^L of 0.019, 0.020, 0.021, 0.022, and 0.023, respectively.

4. Measurement methods

In the present study, we investigate the microstructural evolution of peritectic transition in Fe-C system. Because of the typical peritectic structure that the δ -phase is surrounded by the γ -phase, we measure the temporal change of two parameters: the dynamic contact angle and the equivalent thickness of γ -phase.

In order to facilitate an effective measurement of the contact angle, a sharp-interface analogue is needed. In experiments, the three interface curves between δ -, γ -, and liquid-phases are crossed at a joint point via graphical treatment of the experimental pictures. The three tangent lines at this crossing point for the three interface lines give rise to the contact angle between phases. This is a sharp interface treatment. However, the model in the present study assumes that all interfaces involved are diffuse interfaces with a finite thickness. The phase-field variable (φ_i) varies smoothly from 0 to 1 within the interface. Hence, in this model, the triple junction is expanded to a triple point area, as shown in Fig. 2(a). The interface between phases is given by the contour line of $\varphi_i = 0.5$ ($i = \delta, \gamma$, and L). Mostly, the three contour lines between δ -, γ -, and liquid-phases or the extension of the contour lines cannot pass a single point inside the triple point area and thus, the determination of the contact angle is ambiguous. In literatures [19,50], a circle with the center at the point $\varphi_\delta = \varphi_\gamma = \varphi_L = 1/3$ is drawn and this circle crosses with each interface lines with an intersection point. The contact angle can be measured by connecting the center and each intersection point. But this measurement method is very sensitive to the radius of the selected circle. For this reason, we use the following way to locate a sharp interface from the diffuse-interface profiles. Firstly, we take the level 0.5 contours of all the phase-field variables, which are defined as the interface between each two adjacent phases (see Fig. 2(a)). The three diffuse interfaces form a diffuse triple junction region. The three vertices of this region p_1 , p_2 and p_3 in Fig. 2(a) are identified by the intersections between the contour lines of 0.5. For instance, the point p_1 is the crossing point of the contour lines of $\varphi_\delta = 0.5$ and $\varphi_\gamma = 0.5$.

The black point in the Fig. 2(a), where $\varphi_\delta = \varphi_\gamma = \varphi_L = 1/3$, is defined as the triple junction (tp). The dynamic contact angle of

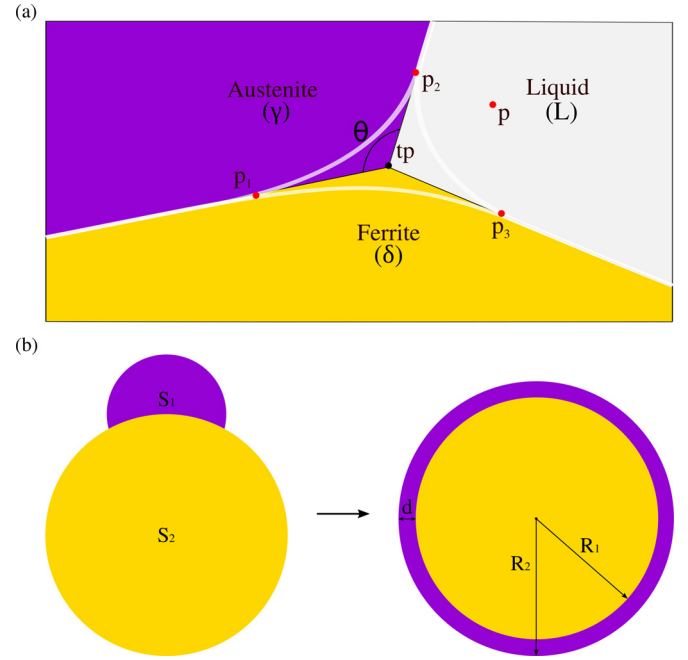


Fig. 2. (a) Level 0.5 contours of all the phase-field variables (white lines) identify a triple region. The three boundary points of this region are marked by red circles and called p_1 , p_2 , and p_3 . The triple junction (tp) is the point where $\varphi_1 = \varphi_2 = \varphi_3 = 1/3$. The dynamic contact angle of γ -phase, θ is defined as the angle between two lines, which are obtained by separately connecting the triple junction with two boundary points. The point p and the triple point tp are symmetric with respect to the connecting line between p_2 and p_3 . (b) Schematic illustration of equivalent thickness of γ phase. (For interpretation of the references to colour in this figure legend, the reader is referred to the web version of this article.)

γ -phase θ is defined as the angle between two lines, which are obtained by separately connecting the triple junction with two vertices (see Fig. 2(a)). It is noteworthy that the phase-field variables are located in the center of each grid cell, which are assigned to be integer values. The exact positions for $\varphi_\delta = \varphi_\gamma = \varphi_L = 1/3$ or $\varphi_i = 1/2$ ($i = \delta, \gamma$, and L) may not locate at the center of the grid cells. In 2D, a bilinear interpolation based on the values of the phase-field variables of four neighbouring cells is used to determine the position of the points p_1 , p_2 , p_3 , and tp (trilinear interpolation in 3D). The resulting points for $\varphi_i = 0.5$ are connected to form the contour line, as schematically illustrated by the white lines in Fig. 2(a). In addition, in the following discussion, we explore the underlying mechanisms of the peritectic transition by analyzing the concentration of the point p , which is chosen to characterize the local liquid concentration in the vicinity of triple point. The point p and the triple point tp are symmetric with respect to the connecting line between p_2 and p_3 (see Fig. 2(a)).

In the peritectic transition process, the γ -particle grows along the interface between liquid and δ -phase. Because of its inhomoge-

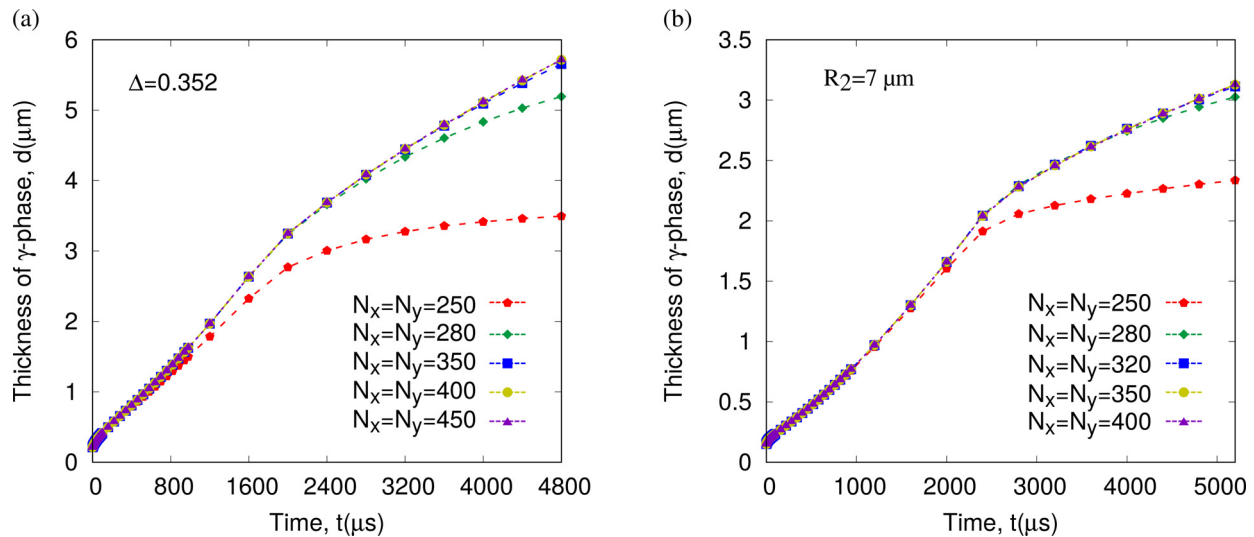


Fig. 3. (a) The thickness of the γ -phase as a function of time for different domain sizes under the same supersaturation $\Delta = 0.352$. (b) The thickness of the γ -phase as a function of time for different domain size, while fixing the size of the δ particle.

neous distribution on the δ -phase, we investigate its development by using an equivalent thickness d .

In Fig. 2(b), the violet γ -phase with an instantaneous surface area of $S_1(t)$ locates on the gold δ -phase at the time step t . The γ -phase is equivalently converted to a ring around the δ -phase with the same area. The equivalent thickness d is calculated by the following equation:

$$d(t) = R_2(t) - R_1(t) = \sqrt{\frac{S_1(t) + S_2(t)}{\pi}} - \sqrt{\frac{S_2(t)}{\pi}}, \quad (20)$$

where $S_1(t)$ and $S_2(t)$ are functions of time and represent the surface area of γ - and δ -particle, respectively.

5. Validation

In order to eliminate the influence of Neumann boundary in simulations on the microstructural evolution, we explore the variations in domain size in this section, while keeping the other simulation conditions fixed.

Fig. 3(a) portrays the time evolution of γ -phase thickness with different domain sizes from $250\Delta x \times 250\Delta y$ to $450\Delta x \times 450\Delta y$ for a constant supersaturation ($\Delta = 0.352$). The space scale of the simulation is $\Delta x = \Delta y = \Delta z = 1 \times 10^{-7}$ m and the physical length is given by $N_x \times \Delta x$. The red, black, blue, yellow, and dark-green lines represent the simulation with domain size of $N_x = N_y = 250, 280, 350, 400$, and 450 , respectively. In all cases, the thickness of the γ -phase layer increases exponentially with time. The underlying physical reason will be discussed later in this paper. With the magnified domain size, a convergence emerges in the simulation results and the simulations with $N_x = N_y \geq 400$ are well converged. It is noteworthy that among all the considered supersaturation, the supersaturation $\Delta = 0.352$ for testing the convergence of the simulations is the largest one, which represents the strongest driving force for the particle growth. The boundary influence recedes with decreasing the driving force. Therefore, we set the domain size with $N_x = N_y = 400$ cells for investigating the influence of liquid supersaturation on the γ -phase thickness. A similar validation is also performed for the study with distinct radius (R_2) of the δ -particle. For the case of δ with the largest initial size ($R_2 = 70$), the simulation results with $N_x = N_y \geq 350$ are converged, which are illustrated in Fig. 3(b). The effect of Neumann bound-

ary weakens with decreasing the initial radius of the δ particle, thereby we explore the γ growth with different initial radii of δ particle in a domain with 350×350 cells.

6. Simulation results and discussion

As observed in experimental microstructures, the austenite platelet (γ) grows along the ferrite (δ)/liquid (L) interface. Aiming to explore the influencing factors of this microstructural evolution during the peritectic transition in carbon steel, we simulate isothermal peritectic solidification of the Fe-C alloy by using the phase-field model in 2-D and 3-D domains. In the 2-D simulations, we investigate the peritectic solidification for the following two cases: (i) on the δ phase with a planar surface and (ii) on the δ phase with a circular surface. In the 3-D simulations, we explore the peritectic transition on the δ phase with different geometries: (a) spherical structure, (b) cylinder structure, and (c) sandglass-shaped structure.

In the following study, we set the initial carbon concentration in the liquid phase c_0^L less than the equilibrium concentration $c_e^{L,\gamma}$ at the temperature $T = 1757$ K, which provides a driving force for the peritectic phase transition.

6.1. 2-D Simulation: Peritectic transition on a planar δ phase

In 2-D simulations, we focus on the growth of austenite on a flat and a circular δ -particle. Fig. 4(a) portrays the microstructural evolution of the peritectic transition on a flat δ -particle. A semi-circular nucleus of the austenite phase with a radius of $2 \mu\text{m}$ is initially placed at the δ -L interface. With time, the austenite phase grows along the δ /L interface in the horizontal direction and its thickness increases in the vertical dimension. Since the austenite phase grows at the expense of the δ and L phases and the δ phase melts at the δ /L interface, the γ / δ interface sinks in the vicinity of the triple point, which is a typical characteristic of peritectic transition. Meanwhile, due to the initial quasi equilibrium setup between the γ and δ phase as well as the relatively small diffusivity in these two solid phases, the interfacial region where the γ and δ phases are in contact at the beginning does not evolve with time. This results in a platform in the middle of the γ phase close to the δ phase.

In order to better explore the mechanism of peritectic transition, we magnify the region in vicinity of the triple junction (see

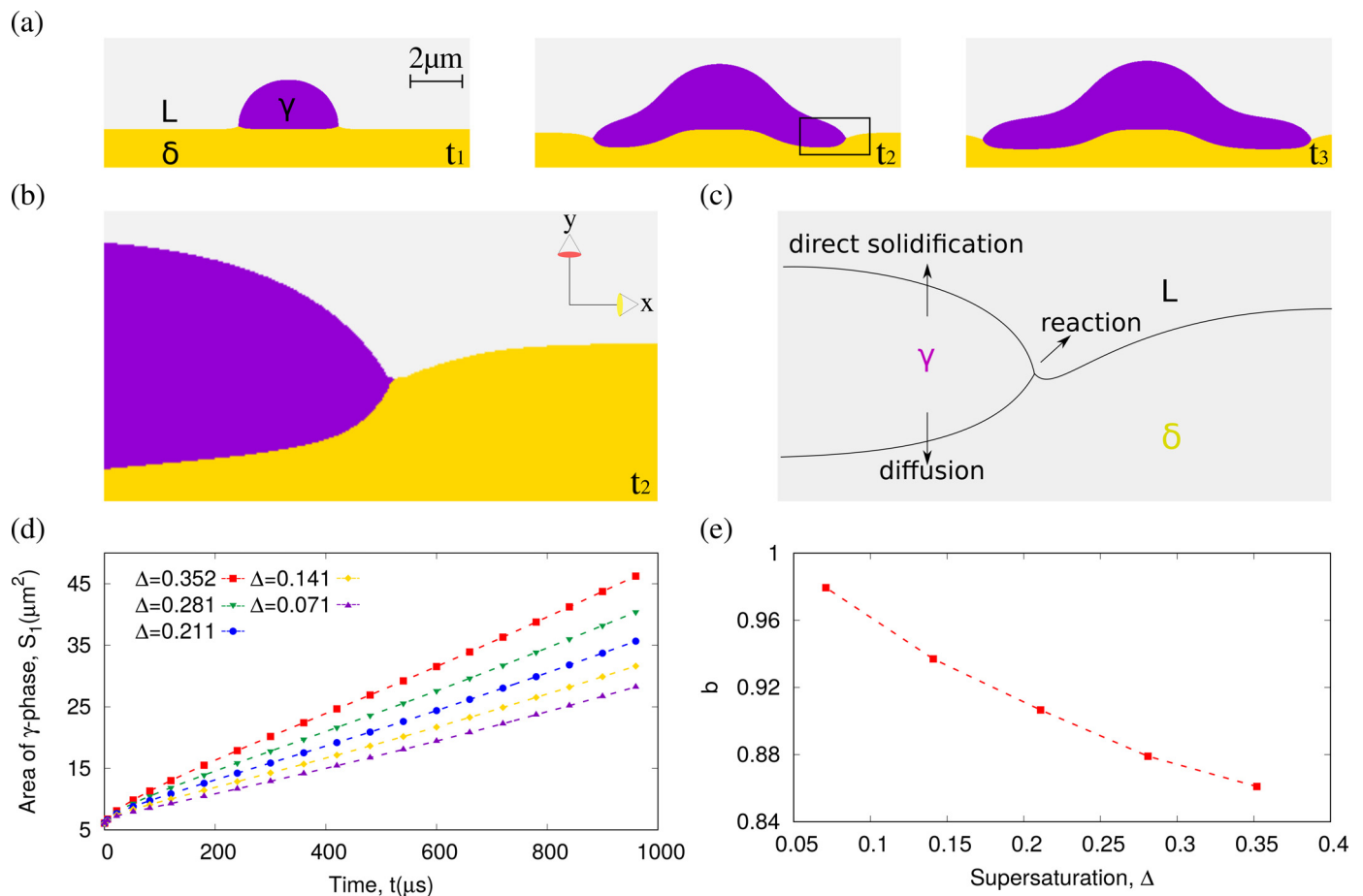


Fig. 4. (a) Microstructural evolution of γ -phase on a planar δ -phase during peritectic phase transition from t_1 to t_3 , where t_1 , t_2 , t_3 represent the time 0, 400 μs , 600 μs , respectively. (b) A magnified region in the vicinity of the triple point which is highlighted in the middle of (a). (c) Schematic diagram for the microstructure of peritectic phase transition near the triple point. (d) The area of γ phase as a function of time for different supersaturation Δ . (e) The growth exponent b for the relation $S_1 = at^b + g$ as a function of Δ .

Table 2
The fitted coefficients for different supersaturation.

Δ	a	b	g
0.352	0.104	0.861	6.388
0.281	0.078	0.879	6.427
0.211	0.055	0.907	6.448
0.141	0.038	0.937	6.445
0.071	0.025	0.979	6.435

Fig. 4(b)). At the front of the austenite phase, the L/δ interface is bent towards the δ -phase. This curved interface indicates the melting of the δ phase during the reaction near the $L/\delta/\gamma$ triple point. This phenomenon is well consistent with previous studies [19,22]. The corresponding schematic diagram of the microstructure near the triple junction is shown in Fig. 4(c). The peritectic solidification involves the peritectic reaction, namely $L + \delta \rightarrow \gamma$ and the subsequent peritectic transformation, namely $\delta \rightarrow \gamma$, $L \rightarrow \gamma$ [51,52]. Fig. 4(d) depicts the area of the γ phase S_1 as a function of time for different supersaturation Δ . The red, green, blue, yellow, and violet lines represent the cases with $\Delta = 0.352$, 0.281, 0.211, 0.141, and 0.071, respectively. In all these 5 cases, S_1 increases exponentially with time, which follows an empirical formulation as

$$S_1 = at^b + g. \quad (21)$$

The fitted coefficients a , b , and g are tabled in Table 2.

A comparison between the five cases shows that a higher supersaturation leads to a faster growth. In order to provide insight into the underlying growth mechanisms, the relationship between the growth exponent b and the supersaturation Δ is shown in Fig. 4(e). With an increase in Δ , b decreases from 0.96 to 0.84. This result indicates that the coefficient b in the case with a higher supersaturation is closer to the theoretical exponent of 0.5 for diffusional growth [53]. A higher supersaturation, as defined in previous section, means a lower carbon concentration in the liquid phase, which provides a larger driving force for the phase transformation at the L/γ interface. With the diminishing supersaturation, the direct solidification of austenite from liquid is inhibited. The whole process is determined by the peritectic reaction. As a result, the coefficient b for the case with supersaturation 0.071 is very close to the exponent of 1 for reaction-controlled limit.

The growth of γ -platelet involves the contributions from peritectic transformation between L/γ and δ/γ interfaces, and from peritectic reaction in the vicinity of the triple point. By analyzing the tip velocity of γ -platelet growing along the L/δ interface, we clarify the influence of various supersaturations on the movement of the triple point, caused by peritectic reaction. Fig. 5 demonstrates the tip velocity of γ -platelet as a function of undercooling in Fe-C alloys with different compositions. Five filled circles, from bottom to top, are obtained by the present simulation and correspond to the five cases with increasing supersaturations shown in Fig. 4(d). The open symbols are the experimental data from Shibata et al. [8] and Grisser et al. [9], which are shown for the

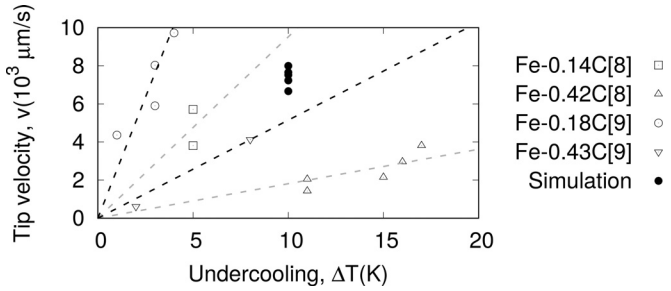


Fig. 5. Tip velocity of γ -phase as a function of undercooling in different Fe-C alloys.

sake of comparison. As aforementioned, the present study focuses on the isothermal peritectic solidification at the 1757 K, which is 10 K below the peritectic temperature (T_p). In order to better compare with experimental data, the mole concentrations for the cases with different supersaturations are converted to the composition in weight percentage of carbon (wt%) based on the initial concentration and volume fraction of each phase in the system, hence the cases with supersaturation of $\Delta = 0.352$, 0.281, 0.211, 0.141, and 0.071 represent Fe-0.341 wt% C, Fe-0.359C, Fe-0.376C, Fe-0.394C, and Fe-0.411C steels, respectively. All five numerical measured values fall within the range of experimental data and the tip velocity of γ -platelet increases with a decrease in the carbon concentration. Good agreement between the numerical results and the experimental data indicates that the present PF-model is capable of quantitatively analyzing the peritectic transition.

6.2. 2-D Simulation: Peritectic transition on a circular δ -phase

As an emblematic peritectic microstructure, austenite surrounds δ -iron, forming a sandwich microstructure: liquid/austenite/ δ . When the δ -phase has a spherical shape, the effect of its curvature on the austenite growth needs to be considered. In this section, we investigate the growth of austenite under different supersaturation and its morphological evolution on ferrite in various sizes.

Fig. 6(a) presents the microstructural evolution of austenite on a δ -particle. Austenite grows along the L/δ interface and thickens gradually with time. When δ -phase is completely encircled by the γ -phase, the $L/\delta/\gamma$ triple point disappears, which leads to the end of peritectic reaction. Subsequently, the peritectic transformation occurs. As a result, γ -phase engulfs the δ -phase and grows in the liquid phase. The whole process is divided into two stages: before (stage 1) and after (stage 2) the disappearance of triple point. Fig. 6(b) illustrates the thickness d of γ -phase, as defined in Eq. (20), as a function of time. The red, green, blue, yellow, and violet dashed lines correspond to the liquid with supersaturation of 0.352, 0.281, 0.211, 0.141, and 0.071, respectively. In all five cases, the size of δ -particle is fixed and the thickness of γ -particle d increases exponentially with time. For each case, d shows two different exponents, by which we classify this process into two stages. For a better discrimination, the stage 2 is indicated by a shading region in Fig. 6(b). A comparison between these five cases shows that with an increase in Δ , the growth rate of the γ -phase enlarges and the dividing point between stage 1 and 2 slightly delays. As discussed in previous section, the supersaturation denotes the deviation of the composition in the liquid from the equilibrium value. This deviation leads to a difference in the grand chemical potential, which provides the driving force for the phase transition. In the following, we define two concentration differences to represent the driving force for the phase transformation at the respective interface. One is $\Delta c^{L,\gamma} = c^L - c_e^{L,\gamma}$ at the L/γ interface; the other is $\Delta c^{L,\delta} = c^L - c_e^{L,\delta}$ at the L/δ interface. Here, $c_e^{L,\gamma} = 0.024032$ and $c_e^{L,\delta} = 0.0203904$ is the equilibrium concentra-

tion in liquid phase with respect to γ and δ phase, respectively. c^L is the carbon concentration in the liquid phase. As illustrated in Fig. 6(c), we use the liquid concentration of the point p, which is defined in Section 4 (see Fig. 2(a)), to characterize the driving force for the morphological evolution of the γ -phase. The red, green, blue, yellow, and violet lines correspond to the five cases in Fig. 6(b). In all these five cases, the composition c oscillates during the peritectic transition and converges after an initial transient time. The convergence of the concentration signifies that the peritectic transition reaches a steady state. At the steady state, the concentration differences $\Delta c^{L,\gamma} < 0$ and $\Delta c^{L,\delta} > 0$ lead to the phase transformation of $L \rightarrow \gamma$ and $\delta \rightarrow L$, respectively. It is noteworthy that the melting of δ ($\delta \rightarrow L$) occurs just ahead of the γ phase due to the local enrichment of concentration in liquid. Comparing these five cases, we find that an increase in Δ leads to an increase in $\Delta c^{L,\gamma}$ and a reduction in $\Delta c^{L,\delta}$. The increase in $\Delta c^{L,\gamma}$ provides a relatively large driving force for the austenite growth towards liquid. The reduction in $\Delta c^{L,\delta}$ inhibits the melting of δ phase, decreasing the rate of the peritectic reaction and thereby delaying the disappearance of the triple junction.

Next, we focus on the influence of the initial radius of δ phase on the peritectic transition. Fig. 6(d) illustrates the normalized thickness of γ phase d_n as a function of time. The red, green, blue, yellow, and violet dashed lines correspond to the δ particle with radius R_2 of 3 μm , 4 μm , 5 μm , 6 μm , and 7 μm , respectively. The supersaturation for these five cases is fixed at $\Delta = 0.141$. The thickness d_n is defined by the following formulation:

$$d_n = \frac{d - d_0}{d_0}, \quad (22)$$

where d is given by Eq. (20) and d_0 represents the initial value at $t=0$. In all five cases, d_n increases with time and the whole process is divided into two stages, which is similar to the previous discussion. In stage 1, these five lines overlap with each other. In stage 2, the five lines separate from each other and are almost parallel, which indicates the same growth rate during the whole peritectic transition. The dividing points between the two stages are marked by the vertical dashed lines. A comparison between these five cases shows that an enlargement of the initial radius of the δ -particle leads to an increase in the migration distance of the triple point, which results in a temporal prolongation of stage 1. In addition, the growth rate of stage 1 is greater than that in stage 2. An increment in d_n is caused by the difference in the growth rate in combination with the extending stage 1, when the δ particle is with a larger initial radius.

In a similar way, Fig. 6(e) depicts the liquid concentration of the point p as a function of time. The red, green, blue, yellow, and violet dashed lines represent the five cases in Fig. 6(d). In all five cases, the concentration almost overlaps with each other, which implies the same driving force for the austenite growth on the δ particle in various radii. When the initial size of the γ phase is fixed, the capillary force remains constant. Therefore, the γ phase grows with the same rate in stage 1 for the δ particle with different radii. Due to the complete encirclement of the δ particle by the γ phase, the triple point disappears. Fig. 6(f) shows the profile of concentration along the black line in Fig. 6(a), corresponding to the three cases with $R_2 = 3 \mu\text{m}$, 5 μm , and 7 μm , respectively. In Fig. 6(f), the concentration $c^{i,j}$ represents the concentration of carbon in the i -phase at the i/j interface ($i, j = \gamma, \delta, \text{ and } L$). As an exemplary explanation, we choose the concentration profile at the time $t = 4800 \mu\text{s}$. The concentration distribution for these three cases displays a similar characteristic. As shown in Fig. 6(f) by the black dashed lines, the local γ concentrations at the γ/L and γ/δ interfaces ($c^{\gamma,L}$ and $c^{\gamma,\delta}$) are the same for these three cases, which is responsible for the same growth rate shown in Fig. 6(d).

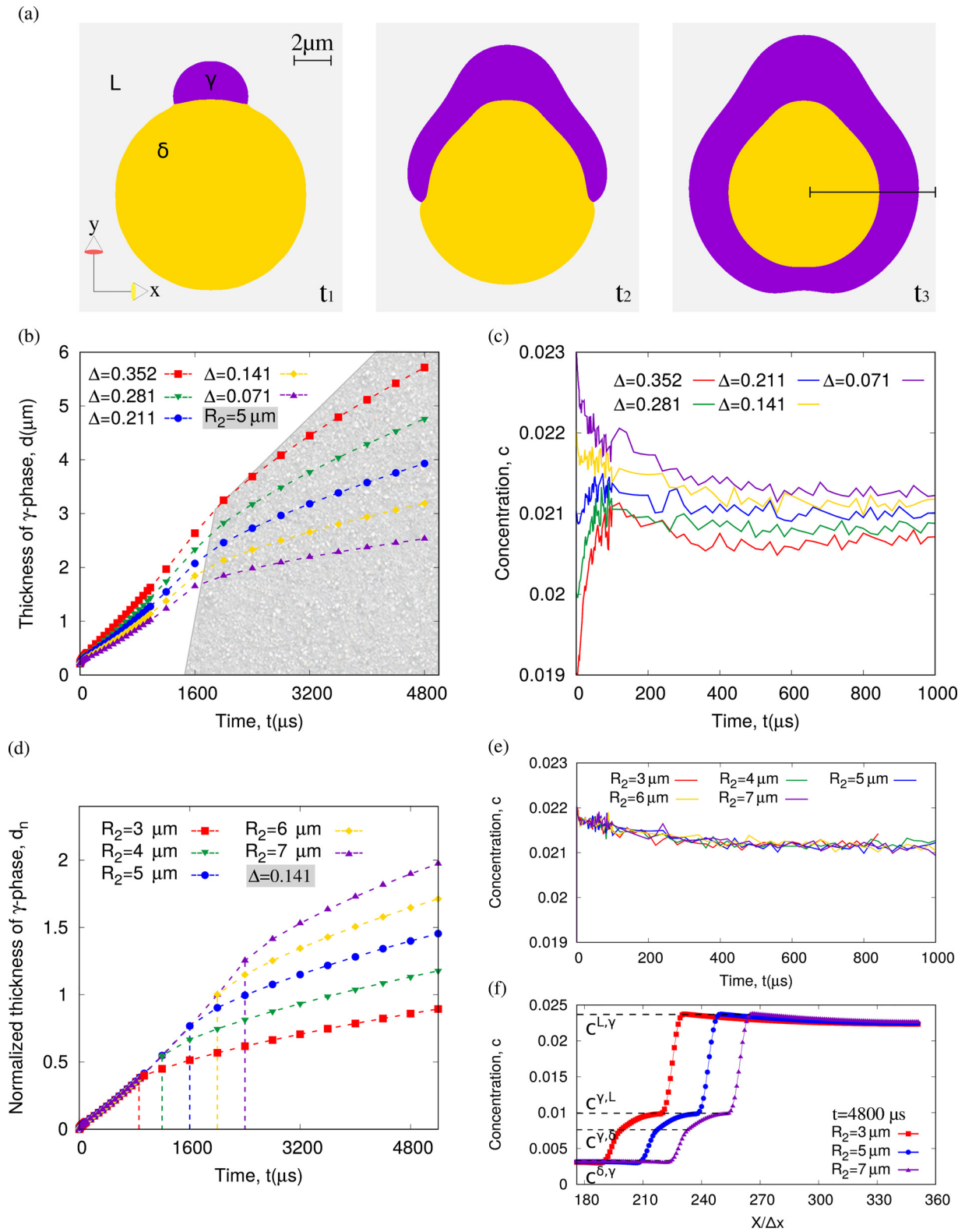


Fig. 6. (a) Morphological evolution of austenite on a circular δ -particle. (b) The thickness d of the γ -phase as a function of time for different supersaturations Δ , where the radius of the δ phase is $5\mu\text{m}$. (c) The liquid concentration of the point p as a function of time for different values of Δ . (d) The normalized thickness d_n of the γ -phase as a function of time for different initial radii of the δ particle, where Δ is set as 0.141 . (e) The liquid concentration of the point p as a function of time for different initial radii of the δ particle. (f) The concentration distribution at the time $t=4800\mu\text{s}$ for different initial radii of δ particle. The concentration $c^{i,j}$ represents the concentration of carbon in the i -phase at the i/j interface ($i, j = \gamma, \delta, \text{ and } L$).

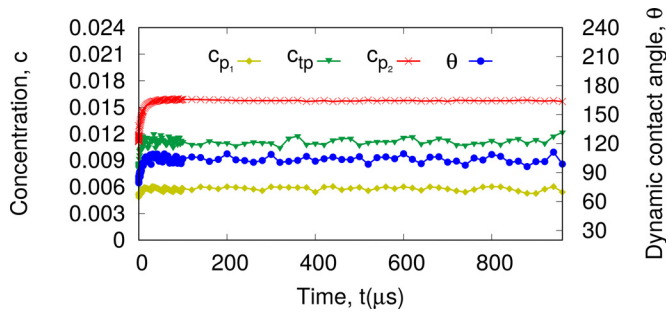


Fig. 7. The dynamic contact angle and the concentrations of the three points p_1 , p_2 , and p_3 as a function of time for the peritectic transition with $\Delta = 0.352$.

6.3. 2-D Simulation: The dynamic contact angle in peritectic transition

According to the previous studies [20], the contact angle between interfaces at a triple junction should follow the thermodynamic equilibrium relation, which is described by Young's law. Typical examples are eutectic and monotectic solidification. However, this is different in the peritectic transition process. In this section, we investigate the dynamic contact angle during the peritectic transition, which is influenced by two factors: the supersaturation Δ and the initial radius R_2 of the δ particle.

Fig. 7 illustrates the time evolution of the dynamic contact angle and the concentration for the peritectic transition on a circular δ -particle ($R_2 = 5 \mu\text{m}$) with $\Delta = 0.352$. The dynamic contact angle (the blue line) increases transiently at the beginning and subsequently converges to about 103° , implying that the peritectic transition reaches a steady state after a certain time. As discussed in Section 3, the dynamic contact angle θ is determined by the positions of the three points, p_1 , p_2 , and tp , which are affected by their relative movement caused by the phase transformation. The

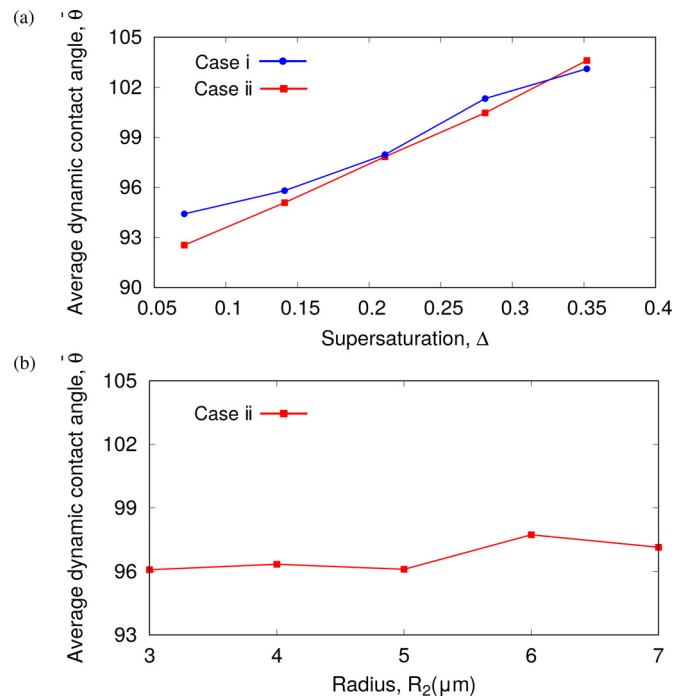


Fig. 8. (a) The average dynamic contact angle as a function of the supersaturation for cases 1 and 2. (b) The average dynamic contact angle as a function of the initial radius R_2 of the δ particle.

concentrations of these three points, which are responsible for the transformation, are depicted in Fig. 7. The yellow, red, and green lines represent the time evolution of the concentration for p_1 , p_2 , and tp , respectively. The concentrations of three points increase simultaneously at the beginning and converge to constants after

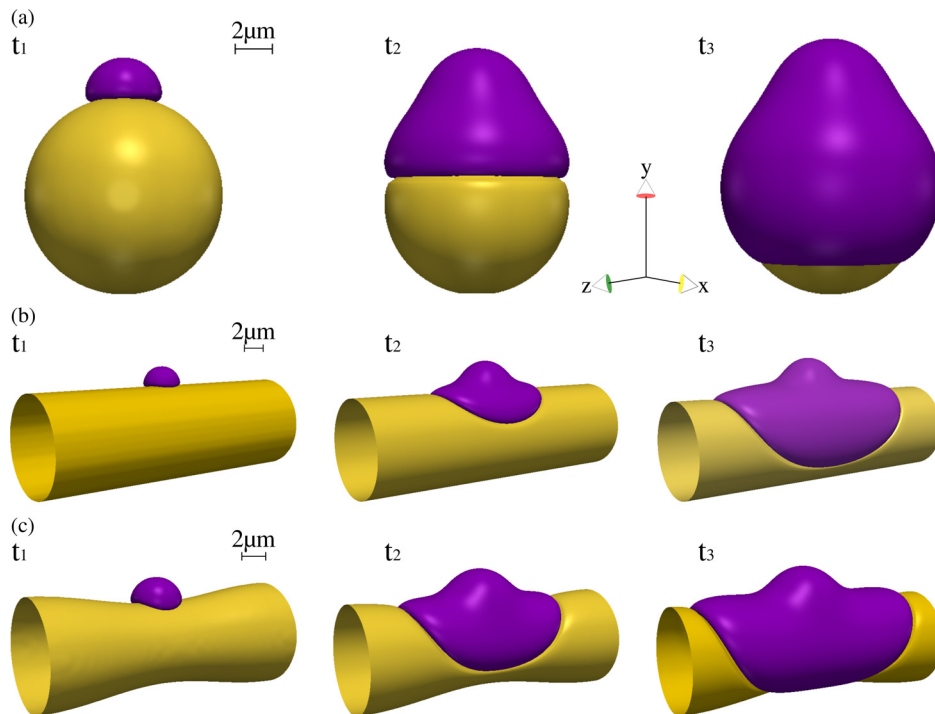


Fig. 9. Morphological evolution of γ phase on δ particle with three different geometries: (a) spherical structure, (b) cylinder structure, and (c) sandglass-shaped structure.

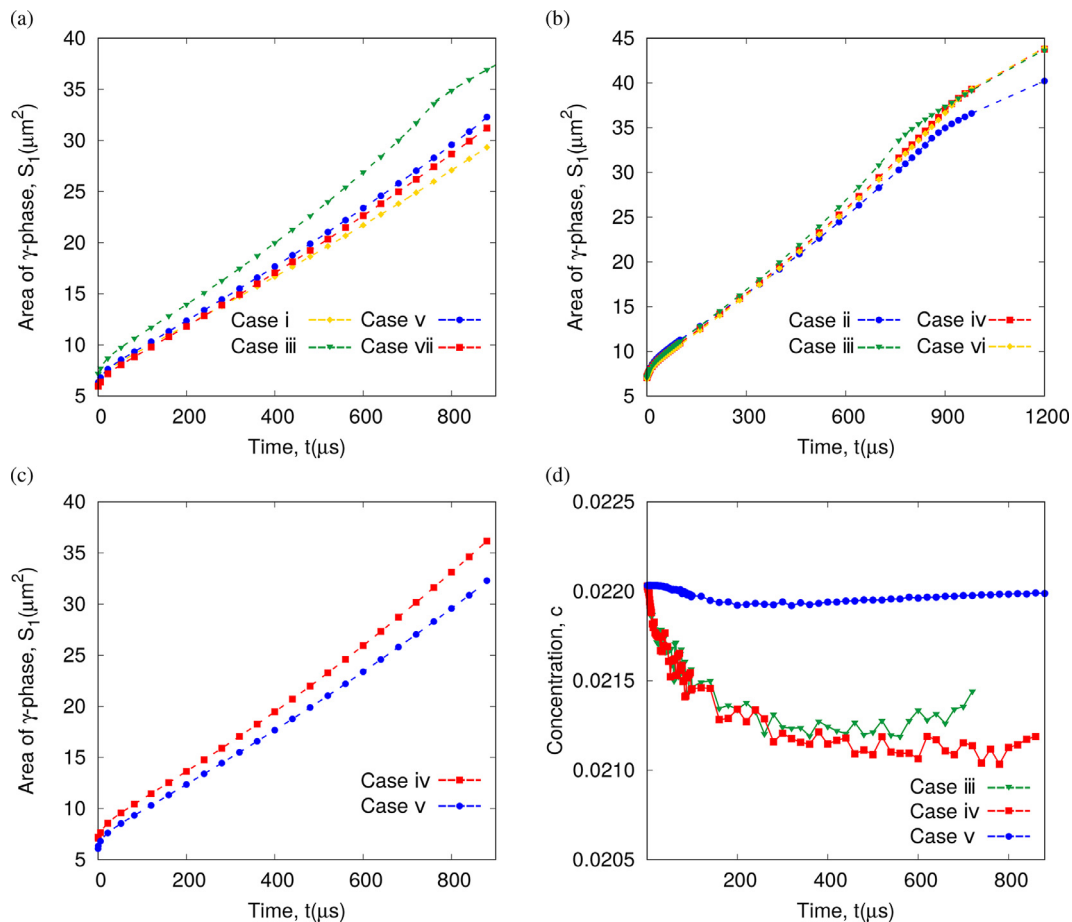


Fig. 10. (a)-(c) The area of the γ phase as a function of time for different cases. (d) The concentration of the point p (see Fig. 2(a)) as a function of time for the cases (iii), (iv), and (v).

reaching the steady state, which shows a quite similar trend to that of the dynamic contact angle. In contrast to the concentration of the other two points, c_{p_2} has a relatively large increase at the beginning. This large increase of c_{p_2} leads to a farther movement of p_2 towards the liquid phase. As a result, the dynamic contact angle θ increases with an enlarging c_{p_2} .

Fig. 8(a) shows the average dynamic contact angle $\bar{\theta}$ as a function of Δ for cases (i) and (ii). In order to eliminate the error caused by the initial setup, we only consider the data at the steady state for the calculation of $\bar{\theta}$. In both cases, $\bar{\theta}$ increases with increasing Δ . As discussed in section 5.2, the increasing supersaturation results in an enlarging phase transformation rate at the L/γ interface towards liquid phase. Meanwhile, the slight increase in the movement rate of the triple point is negligible. Therefore, the dynamic contact angle increases with the supersaturation Δ . The dependence of $\bar{\theta}$ on the initial radius of δ particle R_2 is depicted in Fig. 8(b). With increasing R_2 , $\bar{\theta}$ almost remains constant, which is consistent with the overlapping of concentrations for different R_2 in Fig. 6(e).

6.4. 3-D Simulation: Peritectic transition on δ particle with different geometries

3D simulations are more close to the reality where the mean curvature has an additional contribution. In this section, we simulate the microstructural evolution of γ phase in 3-D domains and investigate the thickness of the production phase and the dynamic contact angle at the triple junction during the peritectic transi-

tion. The differences between 2-D simulation and 3-D simulation are discussed.

Fig. 9 portrays the morphological evolution of peritectic transition on the δ phase with different geometries: (a) spherical structure, (b) cylinder structure, and (c) sandglass-shaped structure. In all three cases, the γ phase is initially set as a hemisphere with a radius of $2 \mu\text{m}$. In (a) and (b), the initial radius of the spherical δ particle and the cylinder δ phase both are $3 \mu\text{m}$. In (c), the shape of the δ phase in the longitudinal dimension is depicted by a cosinusoidal function and the cross section through the center of sandglass is a circle with a radius of $3 \mu\text{m}$.

In order to compare the simulation results with the cases (i) and (ii) in 2-D simulations, which are previously defined in Section 5, we explore the peritectic transition in 3-D for the following five cases: (iii) δ phase with a spherical structure in the x-y plane (Fig. 9(a)), (iv) δ phase with a cylinder structure in the x-y plane (Fig. 9(b)), (v) δ phase with a cylinder structure in the y-z plane (Fig. 9(b)), (vi) δ phase with a sandglass-shaped structure in the x-y plane (Fig. 9(c)), (vii) δ phase with a sandglass-shaped structure in the y-z plane (Fig. 9(c)). In all the cases (iii)-(vii), the γ phase grows on a planar or quasi-planar δ phase in the y-z plane and on a circular δ particle in the x-y plane. The former one is similar to case (i) and the latter one is comparable with case (ii). In all the cases (i)-(vii), the γ phase gradually covers the outer surface of δ phase.

Fig. 10(a) depict the area S_1 of the γ phase as a function of time t for the cases (i), (iii), (v), and (vii). It is noted that case (iii) represents the result in the x-y plane on a circular particle, which

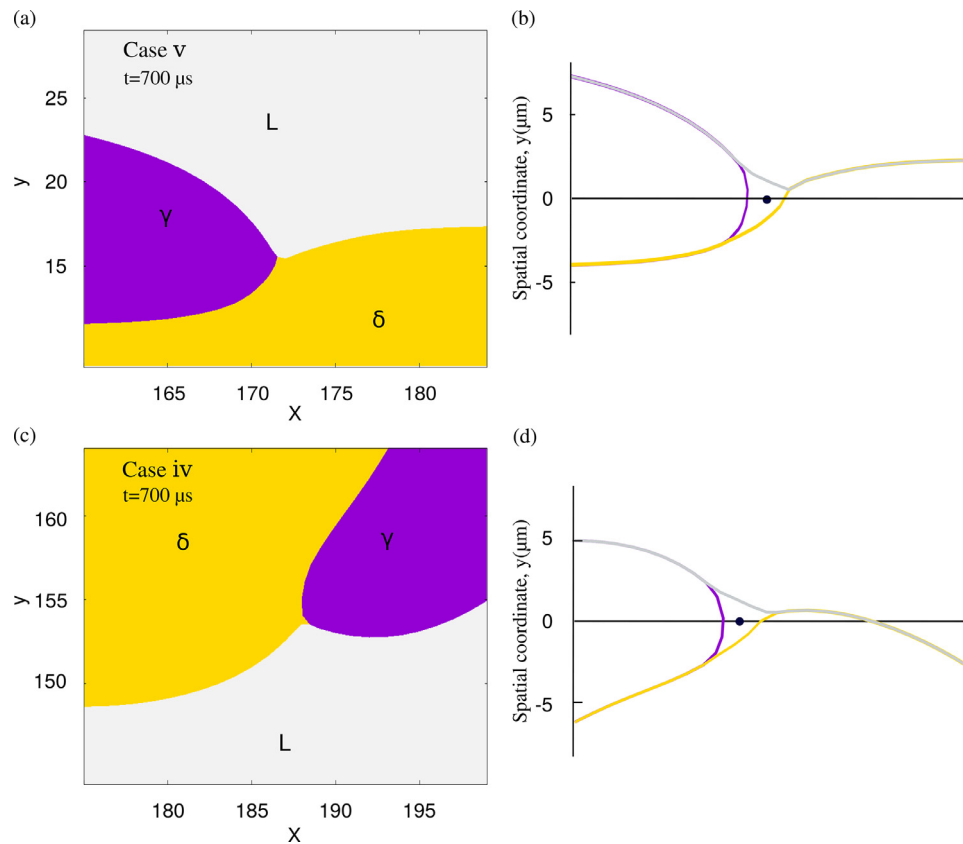


Fig. 11. (a) and (c) The microstructure in the vicinity of triple point at the time $t = 700 \mu\text{s}$ for the cases (v) and (iv), respectively. (b) and (d) The calculated shape of interfaces corresponding to Fig. 11(a) and (c), respectively.

differs from the one on a flat δ phase in the cases (i), (v), and (vii). Hence, the green line shows a different exponent b of t^b from the other three lines. This difference is an evident effect of the curvature. In the cases (i), (v), and (vii), the area S_1 increases with time with an almost identical exponent b . A comparison between these four cases shows that S_1 in 3-D increases faster than the one in 2-D and on a circular surface faster than that on a planar surface.

In Fig. 10(b), the blue, green, red, and yellow lines depict the cases (ii), (iii), (iv), and (vi), respectively. In all four cases, S_1 increases with time and shows obviously different exponents of time in two distinct growing stages, similar to the observation in the Fig. 6(d). A comparison between these four cases demonstrates a similar result that γ phase in 3-D has a larger growth rate than in 2-D. In the 3-D simulations, the γ nucleus is set as a hemisphere with a surface-to-volume ratio (SVR) of $3/R$, whereas in 2-D simulations, the SVR of the semicircular γ particle is $2/R$. Here, R is the radius of the γ particle and is fixed in 2-D and 3-D. The bigger SVR facilitates the peritectic reaction and hence leads to a larger growth rate in 3-D. The red and yellow lines almost overlap with each other, which both are lower than the green line. This implies that the γ phase grows on a cylinder and a sandglass-shaped δ phase with a nearly same rate, which is slower than that on a spherical δ phase. After entering into the stage 2 for the cases (iii), (iv), and (vi), the area S_1 increases with the same growth rate, which is caused by the identical supersaturation. The red and blue lines in Fig. 10(c) represent the cases (iv) and (v), respectively. A comparison between these two cases shows a difference in the growth rate for the γ phase in the x - y and y - z planes.

We explain the underlying mechanism of the difference in the growth rate for different cases by analyzing the concentration of

the point p . Fig. 10(d) exemplifies the concentration as a function of time for the cases (iii), (iv), and (v), which are shown by green, red, and blue lines, respectively. The concentration for case (v) remains almost constant, whereas the concentrations for the cases (iii) and (iv) oscillate around a particular value after an initial transient stage. According to the previous discussion, the growth of the γ phase is controlled by the remelting of δ phase in the vicinity of triple point. The concentration difference $\Delta c^{L,\gamma}$ for the cases (iii) and (iv) is greater than that for case (v), which results in a larger driving force for the phase transformation $L \rightarrow \gamma$. As a result, in cases (iii) and (iv), γ phase grows faster than that in case (v). However, the concentration difference $\Delta c^{L,\delta}$ in the first two cases is smaller than that in the last case and consequently the phase transformation $\delta \rightarrow L$ is inhibited in the former two cases. Fig. 11(a) and (c) depict the microstructure in the vicinity of triple point at the time $t = 700 \mu\text{s}$ for the cases (v) and (iv), respectively. Fig. 11(b) and (d) illustrate the calculated shape of interfaces corresponding to Fig. 11(a) and (c), respectively. In each figure, the violet, yellow, and gray lines represent the contour lines of $\varphi_\gamma = 0.5$, $\varphi_\delta = 0.5$, and $\varphi_L = 0.5$ phase, respectively. In order to facilitate the comparison between the cases (iv) and (v), the shape of interfaces in Fig. 11(d) is rotated until the two points at the γ interface, which are farthest from the triple point, fall on the y -axis. The triple point situates at the x -axis for both cases. In the vicinity of the triple point, a triangular shaped region is surrounded by the interfaces, because the isolines of $\varphi_\alpha = 0.5$ cannot intersect at the triple point. The L/δ interface, which is defined by the coincidence part of yellow and gray lines, curves towards δ phase in Fig. 11(b), indicating the melting of δ , whereas in Fig. 11(d), this interface shows no evident change. This difference in microstruc-

Table 3
Average dynamic contact angle for cases (iii)-(vii).

	Case (iii)	Case (iv)	Case (v)	Case (vi)	Case (vii)
$\bar{\theta}$ (°)	94.18	95.44	96.9	95.12	97.24

ture is attributed to the larger solute enrichment in the vicinity of triple point in case (v), as shown in Fig. 10(d).

The average dynamic contact angle $\bar{\theta}$ is calculated by using the data in the steady state. The angles $\bar{\theta}$ for the cases (iii)-(vii) are tabulated in Table 3. A comparison between these five cases shows that the shape of δ particle has no evident influence on the dynamic contact angle under the same supersaturation.

7. Conclusion and outlook

By using the phase-field method, we have systematically investigated the morphological evolution of peritectic transition in Fe-C binary system through 2-D and 3-D simulations, with inputs from the CALPHAD database. A novel measurement method is proposed to more precisely determine the dynamic contact angle.

The simulation results show that the growth of γ phase on a planar δ phase is affected by the supersaturation Δ and the growth rate increases with Δ . Due to the supersaturation, the migration distance of L/γ interface is larger than that of the δ/γ interface. The tip velocity of γ -platelet, obtained in our simulations, is in concordance with the experimental data, which indicates that the present PF-model can quantitatively investigate the peritectic transition. In addition, the δ/L interface near the $L/\gamma/\delta$ triple point deflects towards the δ phase region, indicating that the melting of δ phase occurs in the vicinity of triple point. The reason is that the local liquid concentration at the triple point is greater than the equilibrium concentration of the liquid phase with respect to the δ phase, but less than the equilibrium concentration of the liquid phase with respect to the γ phase.

Furthermore, we have elucidated that when the γ phase grows on a circular δ particle, the growth rate of γ phase enlarges with Δ and remains constant with an increase in the size of the δ particle. Differing from the γ growth on a planar δ phase, the growth process on a circular δ particle is divided into two stages by the complete engulfment of the δ particle.

In addition, we have measured the dynamic contact angle and found that the average dynamic contact angle increases with the liquid supersaturation and remains almost constant with increasing the radius of the δ phase.

Through the comparison between 2-D and 3-D simulation results, we have clarified that the growth of γ phase in 3-D is faster than in 2-D, as a result of the bigger value of SVR in 3-D. Furthermore, in 3-D simulation, the growth rate of γ phase is unequal in radial and axis direction, due to the asymmetric microstructure.

By simulating the growth of peritectic phase in Fe-C system, we have clarified the mechanisms of peritectic transition with various supersaturation, which should be helpful to understand this complex phase transition in other systems.

Declaration of Competing Interest

The authors declare that they have no known competing financial interests or personal relationships that could have appeared to influence the work reported in this paper.

Acknowledgement

The authors gratefully acknowledge financing of the phase-field modelling of peritectic phase transformation by the Europäis-

cher Fonds für regionale Entwicklung (EFRE) and the Ministerium für Wissenschaft, Forschung und Kunst Baden-Württemberg within the research center ZAFH InSEL.

Furthermore, funding by the German Research Foundation (DFG) in the frame of the Research Training Group 2561: Materials Compounds from Composite Materials for Applications in Extreme Conditions is gratefully acknowledged.

Appendix A. Interface width

The width of the diffuse interface resulting from the present formalism is discussed in this section. The grand potential functional of the binary system for two phases α and β , where $\varphi_\alpha + \varphi_\beta = 1$ and μ is expressed as μ for this binary system, is written as

$$\Omega(\varphi_\alpha, \mu) = \int_V \left[\gamma_{\alpha\beta} \epsilon |\nabla \varphi_\alpha|^2 + \frac{16}{\pi^2} \frac{\gamma_{\alpha\beta}}{\epsilon} \varphi_\alpha (1 - \varphi_\alpha) + \Psi^\alpha(\mu) h(\varphi_\alpha) + \Psi^\beta(\mu) h(1 - \varphi_\alpha) \right] dx. \quad (\text{A.1})$$

In equilibrium, the movement speed of the interface is zero, reading

$$\tau_{\alpha\beta} \epsilon \frac{\partial \varphi_\alpha}{\partial t} = - \frac{\delta \Omega}{\delta \varphi_\alpha} \equiv 0, \quad (\text{A.2})$$

For an one-dimensional setup, the equilibrium equation writes

$$2\gamma_{\alpha\beta} \epsilon \frac{d^2 \varphi_\alpha}{dx^2} = \frac{16}{\pi^2} \frac{\gamma_{\alpha\beta}}{\epsilon} (1 - 2\varphi_\alpha) + \left(\Psi^\alpha(\mu) - \Psi^\beta(\mu) \right) \frac{dh(\varphi_\alpha)}{d\varphi_\alpha}, \quad (\text{A.3})$$

Both sides of Eq. (A.3) multiplying by $\frac{d\varphi_\alpha}{dx}$ and integrating from $-\infty$ to x yield

$$\int_{-\infty}^x \frac{d\varphi_\alpha}{dx} \frac{d^2 \varphi_\alpha}{dx^2} dx = \int_{-\infty}^x \left[\frac{16}{\pi^2} \frac{1}{\epsilon^2} \frac{1 - 2\varphi_\alpha}{2} + \frac{1}{2\gamma_{\alpha\beta} \epsilon} \left(\Psi^\alpha(\mu) - \Psi^\beta(\mu) \right) \frac{dh(\varphi_\alpha)}{d\varphi_\alpha} \right] \frac{d\varphi_\alpha}{dx} dx \quad (\text{A.4})$$

Upon integrating with the conditions $\frac{d\varphi_\alpha}{dx} = 0, x \rightarrow -\infty$ and $h(\varphi_\alpha) = 0$ when $\varphi_\alpha = 0$, the following equation is obtained

$$\left(\frac{d\varphi_\alpha}{dx} \right)^2 = \frac{16}{\pi^2} \frac{1}{\epsilon^2} \varphi_\alpha (1 - \varphi_\alpha) + \frac{1}{\gamma_{\alpha\beta} \epsilon} \left(\Psi^\alpha(\mu) - \Psi^\beta(\mu) \right) h'(\varphi_\alpha). \quad (\text{A.5})$$

The interface width $\Lambda_{\alpha\beta}$ is estimated by

$$\Lambda_{\alpha\beta} = \int_{-\infty}^{\infty} dx = \int_0^1 \frac{1}{\frac{d\varphi_\alpha}{dx}} d\varphi_\alpha. \quad (\text{A.6})$$

Based on Eq. (A.5), the interface width is derived as

$$\Lambda_{\alpha\beta} = \epsilon \int_0^1 \frac{d\varphi_\alpha}{\sqrt{\left[\frac{16}{\pi^2} \varphi_\alpha (1 - \varphi_\alpha) + \frac{\epsilon}{\gamma_{\alpha\beta}} \left(\Psi^\alpha(\mu) - \Psi^\beta(\mu) \right) h'(\varphi_\alpha) \right]}}. \quad (\text{A.7})$$

When there is no driving force between the phases α and β , the difference of the grand chemical potential of two phases $\Delta\Psi = \Psi^\alpha(\mu) - \Psi^\beta(\mu) = 0$ and the interface width is expressed as

$$\Lambda_{\alpha\beta} = \epsilon \frac{\pi^2}{4}. \quad (\text{A.8})$$

The above expression of the interface width is also valid for the phase transition with small driving force. In the same manner, the

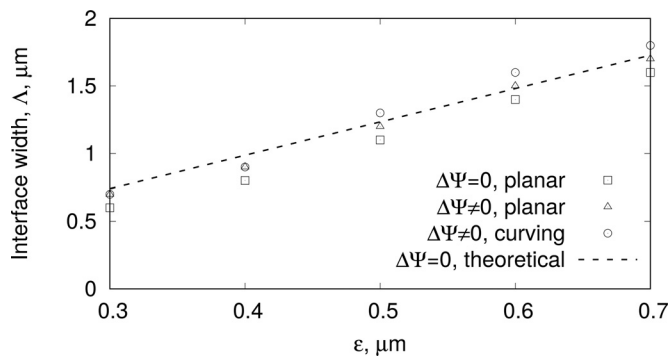


Fig. A.12. The interface width as a function of ϵ .

interfacial energy $\sigma_{\alpha\beta}$ is derived from Eq. (A.3) and written as

$$\sigma_{\alpha\beta} = 2\gamma_{\alpha\beta} \int_0^1 \sqrt{\left[\frac{16}{\pi^2} \varphi_\alpha (1 - \varphi_\alpha) + \frac{\epsilon}{\gamma_{\alpha\beta}} (\Psi^\alpha(\mu) - \Psi^\beta(\mu)) h'(\varphi_\alpha) \right]} d\varphi_\alpha. \quad (\text{A.9})$$

When there is no driving force $\Delta\Psi = 0$ or the contribution from the latter term in Eq. (A.9) is far less than the one from the former term, which is the typical case of equilibrium solidification, we obtain that the physical parameter interfacial energy $\sigma_{\alpha\beta}$ equals the simulation parameter $\gamma_{\alpha\beta}$. For such two cases, the parameters $\sigma_{\alpha\beta}$ and $\Delta_{\alpha\beta}$ are independent from each other. Hence, for the sake of convenience, we set the interface width of all three interfaces with the same value in the present simulations without interfering with the physical values of the interfacial energies.

In the following, we perform 1D simulations to validate the derived equation, Eq. (A.7) with ($\Delta\Psi \neq 0$) and without ($\Delta\Psi = 0$) driving force. Aiming to prove the above theoretical calculation, we simulate a binary phase transition between γ and liquid phases, as an exemplary validation. Considering the influence of the driving force on the interface width, we choose its largest value $\Delta = 0.352$ considered in the present work for the validation. Furthermore, the theoretical derivation is based on the one-dimensional setup, where the curvature effect has not been considered. In particular, non-uniform curvature may lead to different driving force during the time evolution and thus engenders a deviation of interface width from that of a planar interface. In order to show this deviation, we conduct simulations with curving L/γ interface, where the γ phase is set as a circle in the liquid phase with the smallest radius 3 μm , corresponding to the largest curvature in the current work. Fig. A.12 illustrates the relationship between the interface width and the modeling parameter ϵ . The black dashed lines is obtained by the theoretical calculation based on Eqs. (A.8) for $\Delta\Psi = 0$. The triangle and the square symbols correspond to a planar L/γ interface with $\Delta = 0.352$ and $\Delta = 0$, respectively. The circle depicts the cases of curving L/γ interface with $\Delta = 0.352$. Under the influence of the driving force and curvature, the interface width for the cases with same ϵ shows a relatively small difference of 0.1–0.2 μm , corresponding to 1–2 grid cells in our simulations. Good agreement between theoretical calculation and simulation results suggests that the present model can simulate the phase transformation with a specified interface width for a fixed ϵ , when the driving force is relatively small.

References

- [1] R. Kuziak, R. Kawalla, S. Waengler, Advanced high strength steels for automotive industry, *Arch. Civ. Mech. Eng.* 8 (2) (2008) 103–117.
- [2] B. De Cooman, Structure-properties relationship in trip steels containing carbide-free bainite, *Curr. Opin. Solid State Mater. Sci.* 8 (3–4) (2004) 285–303.
- [3] P. Jacques, Transformation-induced plasticity for high strength formable steels, *Curr. Opin. Solid State Mater. Sci.* 8 (3–4) (2004) 259–265.
- [4] A. Grill, K. Sorimachi, J. Brimacombe, Heat flow, gap formation and break-outs in the continuous casting of steel slabs, *Metall. Trans. B* 7 (2) (1976) 177–189.
- [5] M. Suzuki, Y. Yamaoka, Influence of carbon content on solidifying shell growth of carbon steels at the initial stage of solidification, *Mater. Trans.* 44 (5) (2003) 836–844.
- [6] J. Xu, S. He, X. Jiang, T. Wu, Q. Wang, Analysis of crack susceptibility of regular carbon steel slabs using volume-based shrinkage index, *ISIJ Int.* 53 (10) (2013) 1812–1817.
- [7] H.W. Kerr, W. Kurz, Solidification of peritectic alloys, *Int. Mater. Rev.* 41 (4) (1996) 129–164.
- [8] H. Shibata, Y. Arai, M. Suzuki, T. Emi, Kinetics of peritectic reaction and transformation in Fe-C alloys, *Metall. Mater. Trans. B* 31 (5) (2000) 981–991.
- [9] S. Griesser, C. Bernhard, R. Dippenaar, Effect of nucleation undercooling on the kinetics and mechanism of the peritectic phase transition in steel, *Acta Mater.* 81 (2014) 111–120.
- [10] H. Nassar, H. Fredriksson, On peritectic reactions and transformations in low-alloy steels, *Metall. Mater. Trans. A* 41 (11) (2010) 2776–2783.
- [11] F. Wang, B. Nestler, A phase-field study on the formation of the intermetallic Al_2Au phase in the Al-Au system, *Acta Mater.* 95 (2015) 65–73, doi:10.1016/j.actamat.2015.05.002.
- [12] Y. Cai, F. Wang, M. Selzer, B. Nestler, Phase-field investigation on the growth orientation angle of aluminum carbide with a needle-like structure at the surface of graphite particles, *Modell. Simul. Mater. Sci. Eng.* 27 (6) (2019) 065010.
- [13] M. Kellner, J. Htzer, E. Schoof, B. Nestler, Phase-field study of eutectic colony formation in NiAl-34Cr, *Acta Mater.* 182 (2020) 267–277, doi:10.1016/j.actamat.2019.10.028.
- [14] J. Tiaden, B. Nestler, H.-J. Diepers, I. Steinbach, The multiphase-field model with an integrated concept for modelling solute diffusion, *Phys. D* 115 (1–2) (1998) 73–86.
- [15] S. Dobler, T. Lo, M. Plapp, A. Karma, W. Kurz, Peritectic coupled growth, *Acta Mater.* 52 (9) (2004) 2795–2808.
- [16] J. Tiaden, Phase field simulations of the peritectic solidification of Fe-C, *J. Cryst. Growth* 198–199 (1999) 1275–1280, doi:10.1016/S0022-0248(98)01009-4.
- [17] D. Phelan, M. Reid, R. Dippenaar, Experimental and modelling studies into high temperature phase transformations, *Comput. Mater. Sci.* 34 (3) (2005) 282–289, doi:10.1016/j.commatsci.2005.02.006. Computational Microstructure Evolution in Steels
- [18] D. Phelan, M. Reid, R. Dippenaar, Kinetics of the peritectic phase transformation: in-situ measurements and phase field modeling, *Metall. Mater. Trans. A* 37 (3) (2006) 985–994.
- [19] M. Ohno, K. Matsuura, Diffusion-controlled peritectic reaction process in carbon steel analyzed by quantitative phase-field simulation, *Acta Mater.* 58 (18) (2010) 6134–6141, doi:10.1016/j.actamat.2010.07.031.
- [20] M. Hillert, Solidification and casting of metals, *Metals Soc. London* 81 (1979).
- [21] G. Boussinot, E. Brener, D. Temkin, Kinetics of isothermal phase transformations above and below the peritectic temperature: phase-field simulations, *Acta Mater.* 58 (5) (2010) 1750–1760, doi:10.1016/j.actamat.2009.11.017.
- [22] S. Pan, M. Zhu, M. Rettenmayr, A phase-field study on the peritectic phase transition in Fe-C alloys, *Acta Mater.* 132 (2017) 565–575, doi:10.1016/j.actamat.2017.04.053.
- [23] A. Karma, Phase-field model of eutectic growth, *Phys. Rev. E* 49 (1994) 2245–2250, doi:10.1103/PhysRevE.49.2245.
- [24] A.A. Wheeler, G. McFadden, W. Boettinger, Phase-field model for solidification of a eutectic alloy, *Proc. R. Soc. Med. of London. Series A: Math. Phys. Eng. Sci.* 452 (1946) (1996) 495–525.
- [25] I. Steinbach, F. Pezzolla, B. Nestler, M. Seeßelberg, R. Prieler, G.J. Schmitz, J.L. Rezende, A phase field concept for multiphase systems, *Phys. D* 94 (3) (1996) 135–147.
- [26] B. Nestler, A. Wheeler, A multi-phase-field model of eutectic and peritectic alloys: numerical simulation of growth structures, *Phys. D* 138 (1) (2000) 114–133, doi:10.1016/S0167-2789(99)00184-0.
- [27] A. Choudhury, B. Nestler, A. Telang, M. Selzer, F. Wendler, Growth morphologies in peritectic solidification of Fe-C: a phase-field study, *Acta Mater.* 58 (10) (2010) 3815–3823, doi:10.1016/j.actamat.2010.03.030.
- [28] A. Choudhury, B. Nestler, Grand-potential formulation for multicomponent phase transformations combined with thin-interface asymptotics of the double-obstacle potential, *Phys. Rev. E* 85 (2) (2012) 021602.
- [29] Y. Chen, A.-A. Bogno, N.M. Xiao, B. Billia, X.H. Kang, H. Nguyen-Thi, X.H. Luo, D.Z. Li, Quantitatively comparing phase-field modeling with direct real time observation by synchrotron x-ray radiography of the initial transient during directional solidification of an Al-Cu alloy, *Acta Mater.* 60 (1) (2012) 199–207.
- [30] H. Xing, X. Dong, H. Wu, G. Hao, J. Wang, C. Chen, K. Jin, Degenerate seaweed to tilted dendrite transition and their growth dynamics in directional solidification of non-axially oriented crystals: a phase-field study, *Sci. Rep.* 6 (2016) 26625.
- [31] R. Folch, M. Plapp, Quantitative phase-field modeling of two-phase growth, *Phys. Rev. E* 72 (1) (2005) 011602.
- [32] A. Karma, Phase-field formulation for quantitative modeling of alloy solidification, *Phys. Rev. Lett.* 87 (11) (2001) 115701.
- [33] R.E. Johnson Jr, R.H. Dettre, D.A. Brandreth, Dynamic contact angles and contact angle hysteresis, *J. Colloid Interface Sci.* 62 (2) (1977) 205–212.
- [34] P.A. Thompson, M.O. Robbins, Simulations of contact-line motion: slip and the dynamic contact angle, *Phys. Rev. Lett.* 63 (7) (1989) 766.
- [35] Š. Šikalo, H.-D. Wilhelm, I. Roisman, S. Jakirlić, C. Tropea, Dynamic contact angle of spreading droplets: experiments and simulations, *Phys. Fluids* 17 (6) (2005) 062103.

- [36] J. Vallotton, J. Dantzig, M. Plapp, M. Rappaz, Modeling of peritectic coupled growth in Cu-Sn alloys, *Acta Mater.* 61 (15) (2013) 5549–5560.
- [37] H. Ha, J. Hunt, A numerical and experimental study of the rate of transformation in three directionally grown peritectic systems, *Metall. Mater. Trans. A* 31 (1) (2000) 29–34.
- [38] N. Liu, F. Liu, C. Yang, Y. Chen, G. Yang, Y. Zhou, Peritectic solidification of undercooled Fe-Co alloys, *J. Alloys Compd.* 465 (1–2) (2008) 391–395.
- [39] G. Azizi, B.G. Thomas, M.A. Zaeem, Review of peritectic solidification mechanisms and effects in steel casting, *Metall. Mater. Trans. B* 51 (5) (2020) 1875–1903.
- [40] S. Akamatsu, M. Plapp, Eutectic and peritectic solidification patterns, *Curr. Opin. Solid State Mater. Sci.* 20 (1) (2016) 46–54.
- [41] H. Fredriksson, T. Nylen, Mechanism of peritectic reactions and transformations, *Metal. Sci.* 16 (6) (1982) 283–294.
- [42] P. Gustafson, A thermodynamic evaluation of the Fe-C system, *Scand. J. Metall.* 14 (5) (1985) 259–267.
- [43] B. Echebarria, R. Folch, A. Karma, M. Plapp, Quantitative phase-field model of alloy solidification, *Phys. Rev. E* 70 (6) (2004) 061604.
- [44] S.G. Kim, W.T. Kim, T. Suzuki, Phase-field model for binary alloys, *Phys. Rev. W* 60 (6) (1999) 7186.
- [45] A. Karma, W.-J. Rappel, Phase-field method for computationally efficient modeling of solidification with arbitrary interface kinetics, *Phys. Rev. E* 53 (4) (1996) R3017.
- [46] B. Nestler, H. Garcke, B. Stinner, Multicomponent alloy solidification: phase-field modeling and simulations, *Phys. Rev. E* 71 (4) (2005) 041609.
- [47] G.B. McFadden, A. Wheeler, D. Anderson, Thin interface asymptotics for an energy/entropy approach to phase-field models with unequal conductivities, *Phys. D* 144 (1–2) (2000) 154–168.
- [48] S.G. Kim, W.T. Kim, T. Suzuki, Interfacial compositions of solid and liquid in a phase-field model with finite interface thickness for isothermal solidification in binary alloys, *Phys. Rev. E* 58 (3) (1998) 3316.
- [49] J. Monk, Y. Yang, M. Mendelev, M. Asta, J. Hoyt, D. Sun, Determination of the crystal-melt interface kinetic coefficient from molecular dynamics simulations, *Modell. Simul. Mater. Sci. Eng.* 18 (1) (2009) 015004.
- [50] W. Villanueva, W. Boettinger, J. Warren, G. Amberg, Effect of phase change and solute diffusion on spreading on a dissolving substrate, *Acta Mater.* 57 (20) (2009) 6022–6036, doi:10.1016/j.actamat.2009.08.033.
- [51] H. W. Kerr, J. Cisse, G. Bolling, On equilibrium and non-equilibrium peritectic transformations, *Acta Metall.* 22 (6) (1974) 677–686, doi:10.1016/0001-6160(74)90077-7.
- [52] S. Griesser, C. Bernhard, R. Dippenaar, Mechanism of the peritectic phase transition in Fe-C and Fe-Ni alloys under conditions close to chemical and thermal equilibrium, *ISIJ Int.* 54 (2) (2014) 466–473, doi:10.2355/isijinternational.54.466.
- [53] R.W. Balluffi, S.M. Allen, W.C. Carter, *Kinetics of materials*, John Wiley & Sons, 2005.